Proc IMechE Part G: J Aerospace Engineering
():–
©The Author(s) 2010
Reprints and permission:
sagepub.co.uk/journalsPermissions.nav
DOI:
http://mms.sagepub.com

Vortex flow hypothesis for a yawed rotor blade in reverse flow*

Michael Mayo, Vrishank Raghav and Narayanan Komerath†
School of Aerospace Engineering
Georgia Institute of Technology
Atlanta, Georgia 30332

Abstract
Rotating blades at high advance ratios can experience reverse flow, where the freestream flow is directed from the sharp trailing edge of the blade to the blunt leading edge. Better understanding of this flow regime can help advance the design of high-speed rotorcraft. In this work, it is hypothesized that the sharp trailing edge of a reverse flow blade develops an attached vortex in a similar manner to a sharp-edged delta wing. Lift, drag and pitching moment data for a static yawed blade in reverse flow are acquired using a load cell and the lift measurements are compared to predictions made with an adaptation of the Polhamus model. Surface tuft flow visualization confirms the presence of an attached span-wise vortex on the blade. Surface flow behavior is used to explain the behavior of observed aerodynamic loads, and correlations are made to previous results found in the literature. Vorticity transport analysis is used to justify the surface flow behavior variation with yaw angle and angle of attack.

Keywords
Reverse flow, Vortex lift, Yawed wing, Flow visualization, Polhamus, Delta wing

1. Introduction

The advance ratios experienced by the rotor blades of modern helicopters such as the Sikorsky X2 and Eurocopter X^3 can exceed 0.8 (2; 3). Here, advance ratio is defined as the ratio of forward flight speed to the rotational tip speed of the rotor. At these high advance ratios, significant sections of the retreating blade experience reverse flow, characterized by the freestream hitting the geometric trailing edge of the blade first and traveling toward the geometric leading edge. The resultant flow field is not well understood and is characterized by early flow separation, negative lift, and periodic vortex shedding (4). Reverse flow is a major limiter in the design of high-speed rotorcraft. Helicopter designs that attempt to

* Presented at 2013 ASME International Mechanical Engineering Congress & Exposition ((1))
† Corresponding author; e-mail: komerath@gatech.edu

mitigate the effects of reverse flow date back to the early 1970's. Fairchild Republic Division's (5) Reverse Velocity Rotor concept featured a negative pitch angle on the retreating blade in order to achieve a positive angle of attack in the reverse flow regime and airfoils with blunt leading and trailing edges. The more recent Sikorsky X2 Technology Demonstrator (6) has coaxial rotors based on the Advancing Blade Concept (7) platform and also features blunt trailing edge airfoil sections near the blade root.

Wheatley et al. (8) performed force measurements on a Pitcairn PCA-2 autogyro rotor at various pitch settings and advance ratios up to $\mu = 0.7$ and found a negative correlation between lift coefficient and advance ratio. Charles et al. (9) tested a UH-1D rotor at advance ratios up to $\mu = 1.1$ and found that rotor performance predictions broke down at $\mu > 0.5$. They also observed flapping instability and a long transient response to control input at $\mu = 1.1$. MacCloud et al. (10) performed tests on a teetering rotor with a NACA 0012 airfoil at advance ratios up to 1.0 and observed a drop in lift coefficient at high advance ratios. Harris et al. (11) performed correlations studies on these early datasets in 2008 and concluded that OVERFLOW-2 could not accurately predict lift, drag and pitching moments for reverse airfoils and could not be recommended for use at an advance ratio beyond 0.35.

A recent study on a slowed UH-60A rotor performed by Datta et al. (3) showed evidence of reverse chord dynamic stall and large pitch-link load impulses on the retreating side of the rotor disc at advance ratios near unity. Kottapali (12) made initial attempts to predict the blade loads from this study using CAMRAD II, but they showed serious issues at $\mu > 0.8$. Predictions made by Yeo (13) using CAMRAD II showed fair airload and structural load correlation. Potsdam et al. (14) performed coupled CFD and comprehensive analysis on this dataset and predicted unconventional wake patterns and a lower surface vortex on the retreating blade, attributing that to dynamic stall. Pitching moment predictions on the advancing and retreating sides were not encouraging. Lee et al. (15) performed time-averaged force measurements and flow visualization on various airfoil sections in reverse flow and found a drag jump at $\alpha = 180°$ due to the unsteady formation and convection of a large vortex in the wake. Lind et al. (4) also conducted reverse flow studies on static sharp and blunt trailing edge airfoils. They found that the large, negative angles of attack of the inboard section of a rotor in reverse flow causes flow separation and the onset of vortex shedding. It was suggested that the use of a blunt-trailing edge airfoil with a relatively linear lift curve slope would be ideal for the reverse flow regime. However, Lind et al. did not study the reverse flow aerodynamics of static yawed airfoils or finite wings.

1.1. Present Scope and Objectives

To understand and predict the aerodynamic loads on a rotor at high advance ratios, the differences between the static and rotating cases for the blade must be clearly defined. Current prediction technology ranges from the use of static 2D airfoil data, corrected for yaw, to the use of full-scale computational fluid dynamics prediction for the rotating rotor in forward flight. Several issues arise at these two extremes as well as all levels of prediction methods in between. To resolve these issues, a systematic approach is needed. This approach must proceed from experiments on a rotor blade operated as fixed

wing in a wind tunnel, through a range of forward-facing as well as reverse-facing angles of attack, and a variation of sweep through the large range encountered in the rotor case. These results must be understood well from a loads point of view, before going to the rotor case. Accordingly, the first step in this process was the exploratory wind tunnel study performed by Raghav et al. (16) on reverse flow over a static yawed wing and found evidence of vortex-induced lift. Load cell measurements showed higher lift curve slopes for reverse flow test cases when compared to regular flow cases at the same yaw angles, and tuft visualization confirmed the existence of an attached vortex on the rotor blade in reverse flow. In that Note we presented a hypothesis that vortex lift similar to that on the swept leading edge of a delta wing, may be a strong phenomenon both in the case of the yawed reversed-flow static blade, and in the case of the retreating rotor blade.

In this work we present results from further analysis from these experiments, and further experiments over a range of yaw angles. In addition, the vortex flow hypothesis from the previous study is pursued and expanded by using the Polhamus suction analogy (17) for delta wing lift to predict reverse flow lift curves. Drag polars, pitching moments and chordwise center of pressure movement are also analyzed in addition to flow visualization analysis at various yaw angles and Reynolds numbers. Use of a static yawed wing allows rotational effects to be decoupled from the already complex behavior of the reverse flow region. The wing used in this study is part of a two-bladed rotor used in dynamic stall research by Raghav (18). The flow regime is limited to that of low Mach number and moderate chord Reynolds numbers.

1.2. Polhamus suction analogy for yawed rotor blade

The Polhamus suction analogy (17) is adapted for the case of a yawed wing in reverse flow as shown in Equation 1. The predictions are presented in the results and discussion section.

$$C_L = K_p \cdot sin\alpha \cdot cos^2\alpha + \left(K_p - K_p^2 \frac{1}{\pi e AR}\right) \frac{1}{cos\Psi} \cdot cos\alpha \cdot sin^2\alpha \tag{1}$$

The terms on the right-hand side correspond to the lift generated by potential flow and the leading-edge vortex respectively. K_p depends only on the plan-form shape and gives the lift-curve slope from small-perturbation theory for small angles of attack. In this paper, K_p will be set equal to the lift-curve slope of the rotor blade in regular flow for each yaw angle being examined. The delta wing sweep angle Λ is equivalent to the yaw angle Ψ, of the blade used in this work. Oswald's efficiency factor e is calculated using Shevell's method (19).

2. Experimental setup

2.1. Instrumentation and data processing

All experiments were performed in the 2.13m×2.74m John Harper wind tunnel at the Georgia Institute of Technology. A NACA 0013 untwisted rectangular blade with an aspect ratio $AR = 3.49$, a chord $c = 0.178$ m, and a span $b = 0.622$ m was set up as shown in Fig. 1. Stepper motors were used to control pitch and yaw. A 6-DOF load cell was used to measure

Table 1. Test matrix for experiments

Test	Flow Type	Data Acquired	Ψ and α	$Re(\times 10^5)$
1	Regular Flow	Validation	$0^\circ \leq \Psi \leq 60^\circ$, $0^\circ \leq \alpha \leq 30^\circ$	1.7
2	Reverse Flow	Lift, Drag, Pitching Moment	$-60^\circ \leq \Psi \leq 60^\circ$, $180^\circ \leq \alpha \leq 210^\circ$	1.7, 3.0
3	Reverse Flow	Flow Visualization	$\Psi = \pm 30, \pm 45$, $180^\circ \leq \alpha \leq 220^\circ$	1.7, 3.0

aerodynamic loads. A 5Hz low pass digital filter removed noise, and a calibration matrix converted the filtered voltage values into forces and moments. Please refer to Raghav et al. (16) for further details of the instrumentation and data processing.

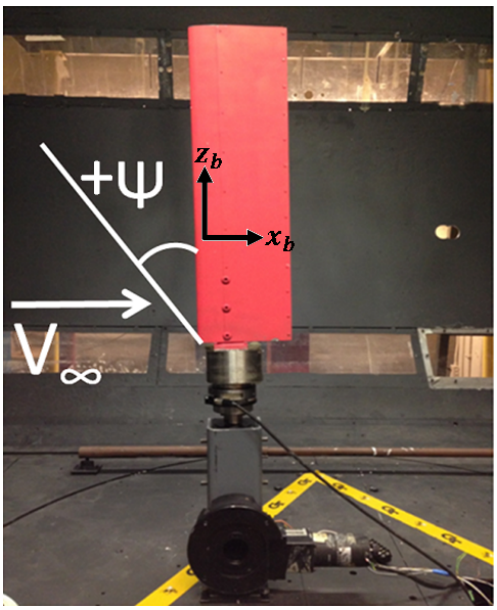

Fig. 1. Side view of the rotor setup in the wind tunnel, where x_b and z_b are blade fixed coordinates)

2.2. Flow and test conditions

The experiments were performed at two Reynolds numbers of 1.7×10^5 and 3.0×10^5 at yaw angles ranging from $\Psi = -60^\circ$(backwards yaw) to $\Psi = 60^\circ$(forwards yaw). The test cases are summarized in Table 1 and described below:

1. The first test validated the experimental method (16) by comparing results for regular flow against published data.

2. The second test acquired lift, drag and pitching moment data for the rotor blade in reverse flow at two Reynolds numbers and various yaw angles. Angle of attack(α) resolution was lower in the linear region of the lift curves and higher near the stall region.

3. The third test consisted of surface flow visualization using tufts at two Reynolds numbers and various yaw angles. The rotor blade was pitched through the angle of attack range in increments of 5°.

2.3. Error analysis

The total error in measurement of the aerodynamic load coefficients was computed to be $\pm 1.61\%$ in the worst case. The total error was computed using the individual errors of the parameters listed in Table 2. The ensemble averaged data are repeatable with a standard deviation within 4.5% of the measured average loads. The blade airfoil contour was measured at 18 different locations across the span of the blade to quantify the difference from NACA0013 coordinates. The root mean square error for the difference was less than 0.1% of the chord.

Table 2. Summary of errors

Parameter	Error Estimate
Density	0.03%
Velocity	0.04%
Reynolds number	± 470
Load cell calibration	$\pm 1.37\%$
Yaw angle	$\pm 0.05^\circ$
Angle of attack	$\pm 0.01^\circ$

3. Aerodynamic loads

3.1. Lift

Lift curve slopes for the reverse flow regime at positive and negative yaw angle and two different Reynolds numbers are shown in Fig. 2 along with forward yaw regular flow lift curve slopes at Re = 1.7×10^5. Figure 1 defines the positive (forward) and negative (backward) yaw angles. Lift curve slopes were calculated using the linear region in the equivalent α range of $0^\circ - 10^\circ$. The occurence of stall near $\alpha = 10^\circ$ in both regular and reverse flow regimes agrees with Lind et al. (4) for a NACA 0012 airfoil in regular and reverse flow and with NACA 0012 reverse flow data collected by Critzos et al. (20) in the Langley low-turbulence tunnel. Raghav et al. (16) showed that the regular flow lift curve slopes follow the $\cos^2\Psi$ fit predicted by cross-flow equivalence (21).

The lift curve slopes for the forward yaw reverse flow cases are slightly higher than the corresponding regular flow lift curve slopes, which suggests that there is an extra source of lift in the reverse flow regime. The difference in the regular and reverse flow lift curves seen in this study correlates well with the difference in lift coefficient seen by Bartlett (22) for beveled and rounded wings with sweepback angle. The lift curve slopes at Re = 3.0×10^5 are slightly higher than the ones at Re = 1.7×10^5, which suggests that Reynolds number does have an effect on aerodynamic loads for a rotor blade in the reverse flow regime. The difference between the two Reynolds numbers is small and even non-existent for certain yaw angles, which supports the suggestion made by Lind et al. (4) that the aerodynamic forces in reverse flow are less dependent on Reynolds number due to early separation.

The backward yaw lift curve slopes do not follow the expected $\cos^2\Psi$ fit, and Reynolds number does appear to have more effect on the lift curve slopes at $\Psi = -15^\circ$ and $\Psi = -30^\circ$ when compared to forward yaw angle cases. Possible

explanations for this behavior are the different orientation of the mount and wingtip in the backward yaw case - this is further examined in the flow visualization section.

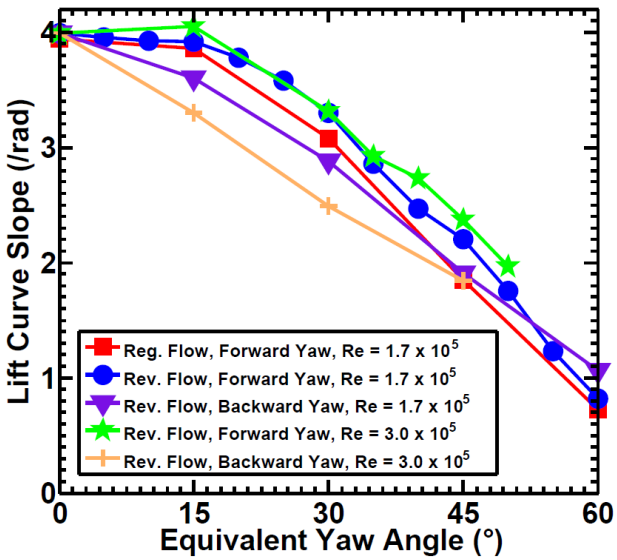

Fig. 2. Lift curve slopes at various Ψ and Re (Ψ negative for backward yaw)

3.2. Predictions using Polhamus suction analogy

The Polhamus suction analogy described in section 1.2 was used to predict lift curves for the reverse flow rotor blade at Re = 1.7×10^5 and forward yaw values of $\Psi = 0°, 15°, 30°, 45°$, and $60°$. These yaw values were chosen because they allowed the K_P term in the vortex lift equation to be matched to the lift curve slopes obtained from the regular flow validation trials. Figure 3(a) compares the predictions made by the vortex lift model at $\Psi = 45°$ and Re = 1.7×10^5 to experimental data. The solid line is the prediction made using the full equation 1, and the dashed line is the prediction made using equation 1 with K_v (second term on the right hand side) set to zero. The dashed line corresponds to lift predicted by potential theory only. The full vortex lift model predicts the lift coefficient with good accuracy up until $\alpha = 195°$, where the experimental lift curve begins to more closely follow the potential prediction. In reality, at higher angle of attack the vortex tends to burst (23) and the measured lift will decrease. However, the current mathematical model does not account for the vortex burst phenomenon. This is reconciled in the surface flow visualization section 4, where vortex burst is observed at higher angle of attack. It should be noted that the experimental lift curve is higher than the potential prediction well after diverging from the vortex model, which may signify that some vortex lift is being generated well after breakdown begins.

Lift curve slopes were calculated using the lift curve predictions generated by the vortex lift model and are compared to experimental data in Figure 3(b). The vortex lift predictions are fairly accurate for $\Psi \geq 30°$. The over-prediction at lower Ψ stems from the fact that the Polhamus equation for low aspect ratio delta wings suffers at low Ψ values which correspond to the leading edge sweep of a high aspect ratio delta wing.

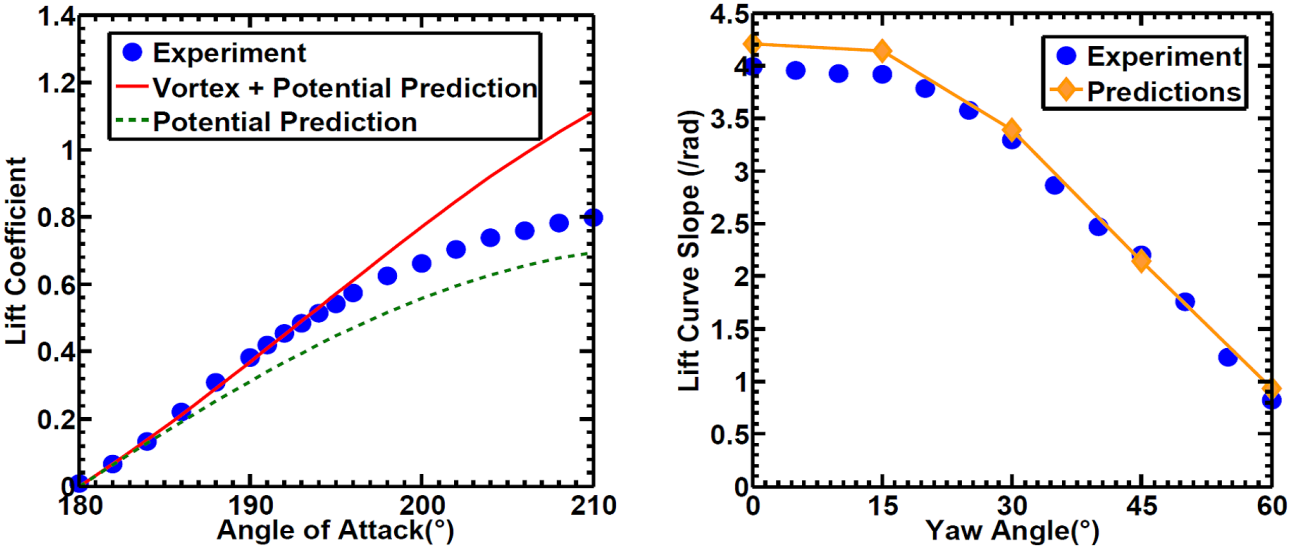

(a) Lift curves for $\Psi = 45°$ produced by vortex lift model and experiment

(b) Lift curve slopes obtained from vortex lift model and experiment at Re = 1.7×10^5

Fig. 3. Lift predictions using the Polhamus model for a yawed blade in reverse flow

3.3. Drag and pitching moment

Drag polars for the regular and reverse flow regime at $\Psi = 30°$ are shown in Figure 4(a). The drag polars at this Ψ are fairly representative of drag polars at other Ψ. The L/D ratios are higher in the regular flow cases. This agrees with results for delta wings, where a sharp-edged delta wing has a lower L/D than a delta wing with a rounded leading edge (24). The regular flow L/D ratio at $\alpha = 10°$ is almost twice as high as the corresponding reverse flow L/D. This result agrees with that discussed by Lind et al. (4) showing that a NACA 0012 airfoil in reverse flow would produce almost twice as much drag at the stall angle while still having the same $C_{L_{max}}$ as a regular flow airfoil.

The reverse flow pitching moments were proportional to lift in the linear region of the lift curve. A plot of C_L and C_M at $\Psi = 45$ for Re = 1.7×10^5 and 3.0×10^5 is shown in Figure 4(b). The non-zero, negative pitching moment in the linear lift region suggests that the center of pressure was located closer to the effective leading edge (i.e., the sharp edge). The chordwise center of pressure was computed from the normal aerodynamic force using the lift and drag measurements as given by equation 2, and the measured pitching moment.

$$N = Lcos(\alpha) + Dsin(\alpha) \tag{2}$$

It should be noted that the resultant chordwise center of pressure location is an average over the span of the blade. The chordwise center of pressure locations for various forward yaw angles at Re = 1.7×10^5 and Re = 3.0×10^5 are shown in Figures 5(a) and 5(b) respectively. A 0.75c location on the plot corresponds to the quarter chord of the reverse airfoil. Data points derived from lift values lower than 0.3N were omitted due to high uncertainty.

Both plots show that at low Ψ, the center of pressure is even closer to the effective leading edge. A possible reason for this trend is discussed in the flow visualization section. The approximate 0.75c center of pressure location for both plots agrees with data collected by Datta (3). For Re = 1.7×10^5, the center of pressure locations start near 0.7c and move toward the effective leading edge as α is increased. Beyond the linear lift region, the center of pressure moves toward the effective trailing edge and eventually settles near 0.75c at $\alpha = 200°$. The Re = 3.0×10^5 cases show a different trend, with center of pressure locations that start closer to the effective leading edge and move toward the effective trailing edge as α is increased, eventually settling near 0.75c. Reasons for the center of pressure movement will be discussed in the flow visualization section.

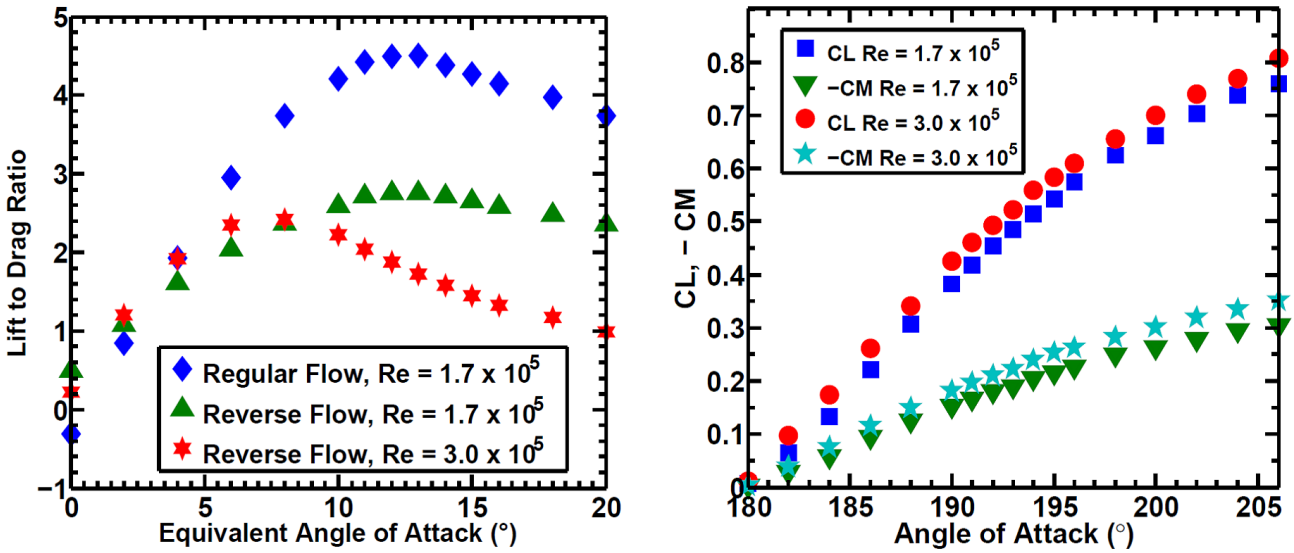

(a) Drag polars at $\Psi = 30°$ ($\alpha = 180° - 200°$ for reverse flow cases)

(b) Variation of lift and pitching moment at $\Psi = 45°$ (pitching moment negative about z_b axis)

Fig. 4. Drag and pitching moment data for regular and reverse flow cases

4. Surface flow visualization

Surface flow visualization was performed using tufts attached to the suction side of the rotor blade. The tufts were 2.5 cm long pieces of yarn taped at 2.5 cm spacing, forming a grid over the entire suction side of the blade. A high definition camera was used to record the visualization. These experiments were performed at Re = 1.7×10^5 and Re = 3.0×10^5 at $\Psi = 30°, 45°, -30°$, and $-45°$. The blade was pitched through various α in increments of $5°$. Reynolds number had little effect on the surface flow patterns. However, large differences in surface flow pattern were observed between forward and backward yaw cases. Hence only one Reynolds number case Re = 1.7×10^5 is discussed in detail.

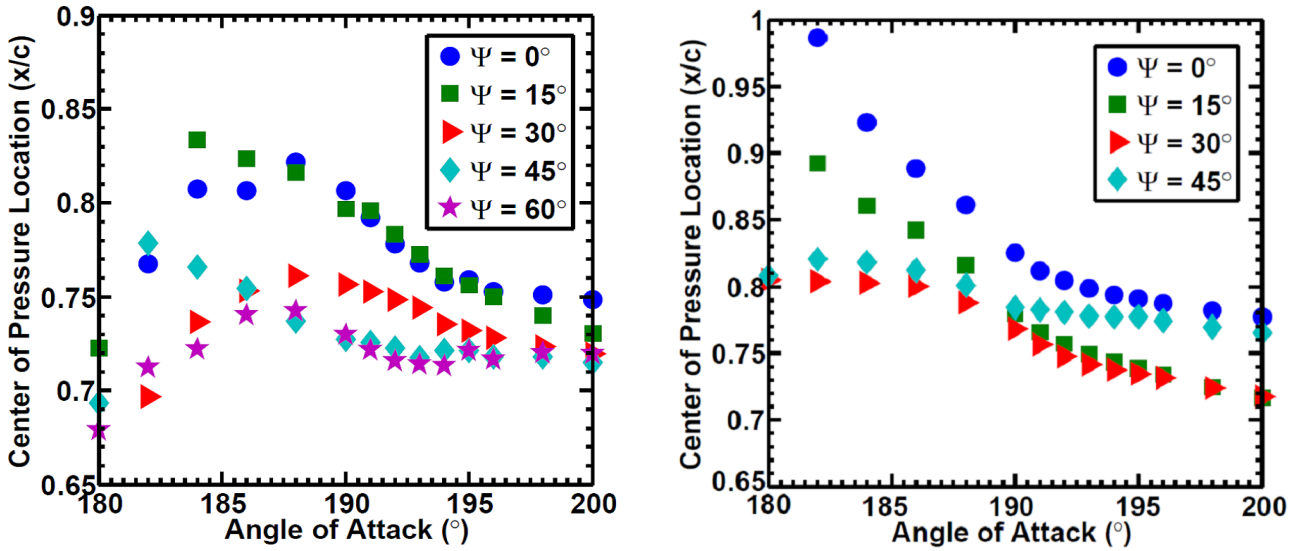

(a) Re = 1.7×10^5 (b) Re = 3.0×10^5

Fig. 5. Variation of chordwise center of pressure location with α at various Ψ

4.1. Forward yaw Re = 1.7×10^5

A. $\Psi = 45°$

Pictures of tuft flow visualization taken at $\Psi = 45°$ and Re = 1.7×10^5 are shown in Figures 6(a)– 6(d). At $\alpha = 185°$ the tufts are mostly attached, but there are a few tufts at the effective leading edge moving in a clockwise, conical rotation pattern when looking from upstream. These rotating tufts are indicative of a leading edge vortex beginning to form. There are also some rotating tufts at the blade tip, indicating the existence of a tip vortex interacting with the freestream. As the blade is pitched to $\alpha = 190°$, the leading edge vortex grows along the span. The rapid growth of the vortex as α increases from $5° - 10°$ correlates well with the large momentum deficit increase seen by Lind et al. (4) for a NACA 0012 airfoil at $\alpha = 189°$. In addition, there is a small region of the tufts exhibiting chaotic motion near the blade root, a characteristic of separated flow, indicating a vortex breakdown region. The vortex breakdown may be attributed to the adverse pressure gradient caused by the mount at the blade root. As the blade is pitched to $\alpha = 195°$, the vortex breakdown region grows larger, which correlates well with the divergence of the experimental lift curve from vortex lift theory seen in Figure 3(a). By $\alpha = 215°$, the leading edge vortex is almost completely broken down and there is only a small region of attached flow between the remnants of the leading edge vortex and the tip vortex region.

In the aerodynamic loads section we discussed the center of pressure on the yawed blade in reverse flow. The physical reasoning for the variation of the center of pressure with angle of attack is now reconciled with the flow visualization experiments. The growth of the leading edge vortex could explain the center of pressure movement seen in Figure 5(a). As the vortex becomes significant at $\alpha = 185°$, the center of pressure would shift toward the location of the vortex at the effective leading edge. As the vortex grows along the span and reaches the effective trailing edge, the center of pressure would "follow" the mean position of the leading edge vortex toward the effective trailing edge, eventually settling near

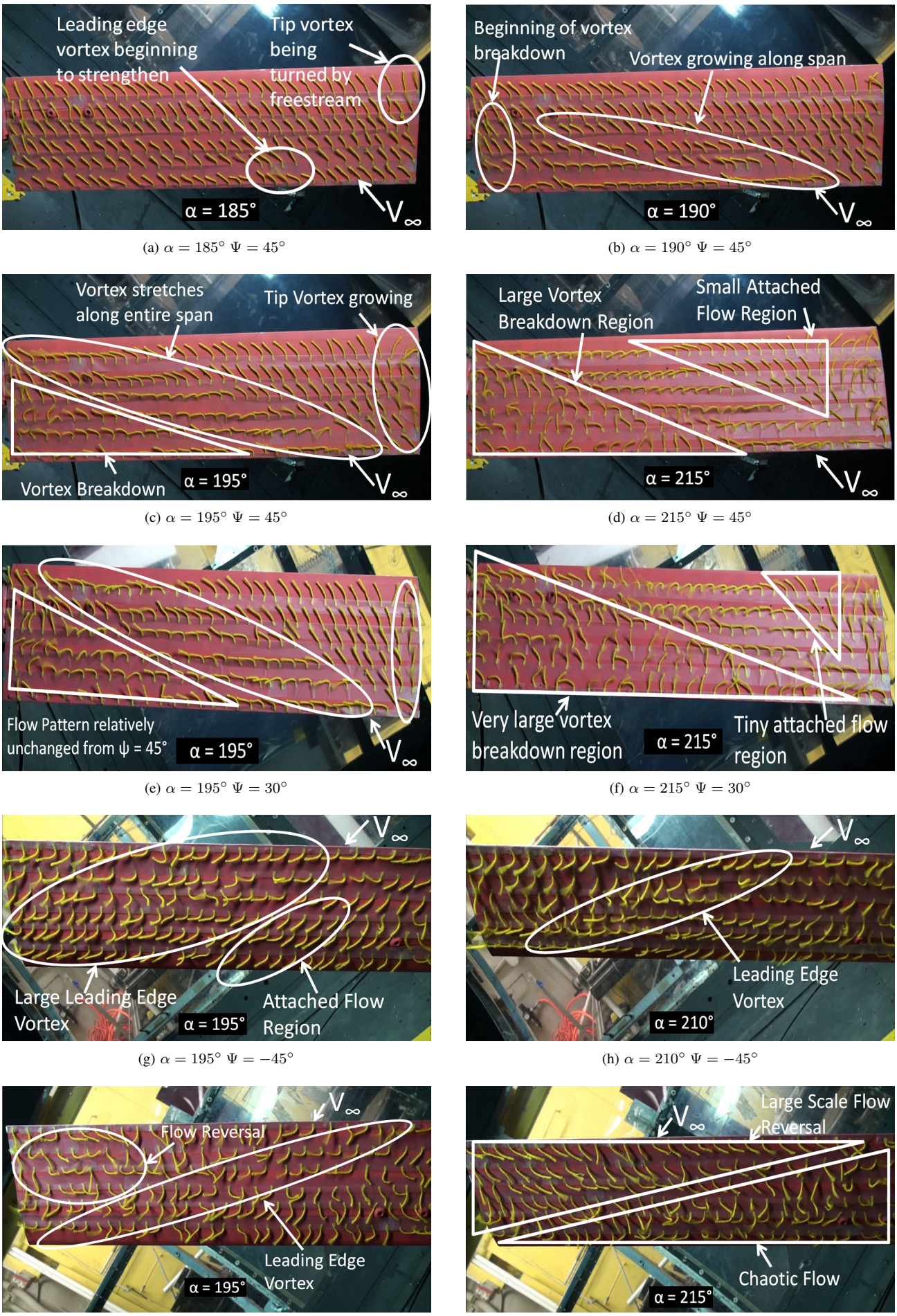

(a) $\alpha = 185^\circ$ $\Psi = 45^\circ$

(b) $\alpha = 190^\circ$ $\Psi = 45^\circ$

(c) $\alpha = 195^\circ$ $\Psi = 45^\circ$

(d) $\alpha = 215^\circ$ $\Psi = 45^\circ$

(e) $\alpha = 195^\circ$ $\Psi = 30^\circ$

(f) $\alpha = 215^\circ$ $\Psi = 30^\circ$

(g) $\alpha = 195^\circ$ $\Psi = -45^\circ$

(h) $\alpha = 210^\circ$ $\Psi = -45^\circ$

(i) $\alpha = 195^\circ$ $\Psi = -30^\circ$

(j) $\alpha = 215^\circ$ $\Psi = -30^\circ$

Fig. 6. Tuft visualization at Re = 1.7×10^5

the 0.75c point. The vortex breakdown region is mainly confined to an area near the effective leading edge of the blade. The location of the vortex breakdown region near the effective leading edge could explain why the chordwise center of pressure appeared to be farther from the effective leading edge for higher Ψ cases in Figure 5(a) and Figure 5(b). The breakdown region would be expected to produce minimal or no lift, which would shift the chordwise center of pressure toward the effective trailing edge. The lower Ψ test cases would not develop a large vortex breakdown region because there would be less spanwise flow and a smaller adverse pressure gradient at the blade root, so the center of pressure would not be shifted as far toward the effective trailing edge.

It is worth noting that the position and shape of the attached span-wise vortex closely resembles that of the lower surface vortex predicted by Potsdam et al. in Figure 25 (14), which was attributed to "reverse-chord dynamic stall". The similar vortex observed in this experiment on a static yawed blade suggests that the vortex predicted by Potsdam et al. may not be an artifact of rotation. Based on prior flow visualization experiments Raghav et al. (16) proposed a flow topology for a blade in forward yaw in reverse flow regime.

B. $\Psi = 30°$

Pictures of tuft flow visualization taken at $\Psi = 30°$ and Re = 1.7×10^5 are shown in Figure 6(e) and Figure 6(f). At $\alpha = 195°$ the observed flow pattern is very similar to the one seen at $\Psi = 45°$, but at $\alpha = 215°$ a much larger vortex breakdown region is observed. The attached flow region is also much smaller than the one observed for $\Psi = 45°$. Reasons for these differences will be discussed in later sections.

4.2. Backward yaw Re = 1.7×10^5

A. $\Psi = -45°$

Pictures of tuft flow visualization taken at $\Psi = -45°$ and Re = 1.7×10^5 are shown in Figure 6(e) and Figure 6(f). At $\alpha = 195°$ the tuft behavior suggests that a large leading edge vortex is present, and no significant signs of vortex breakdown are observed. Unlike the forward yaw $\Psi = 45°$ case, mount obstruction does not impede the growth of the leading edge vortex by creating an adverse pressure gradient. A smaller adverse pressure gradient may be present at the rotor blade tip due to a tip vortex, but at this angle of attack it appears that the spanwise flow mostly negates the effect of any tip vortex. The attached flow region is fairly small, which is partly due to mount interference near the blade root. At $\alpha = 210°$ the leading edge vortex more closely resembles the one seen at $\Psi = 45°$.

B. $\Psi = -30°$

Pictures of tuft flow visualization taken at $\Psi = -30°$ and Re = 1.7×10^5 are shown in Figure 6(e) and Figure 6(f). At $\alpha = 195°$ a leading edge vortex is apparent, but it does not appear to have much strength. Some tufts near the blade tip signify a reversal of the expected span-wise flow direction. At $\alpha = 215°$ the rotor blade planform can be evenly

divided into two regions: a region where the flow appears to be fairly laminar but directed toward the root of the blade in opposition to the freestream flow, and a region of chaotic flow.

4.3. Flow topology

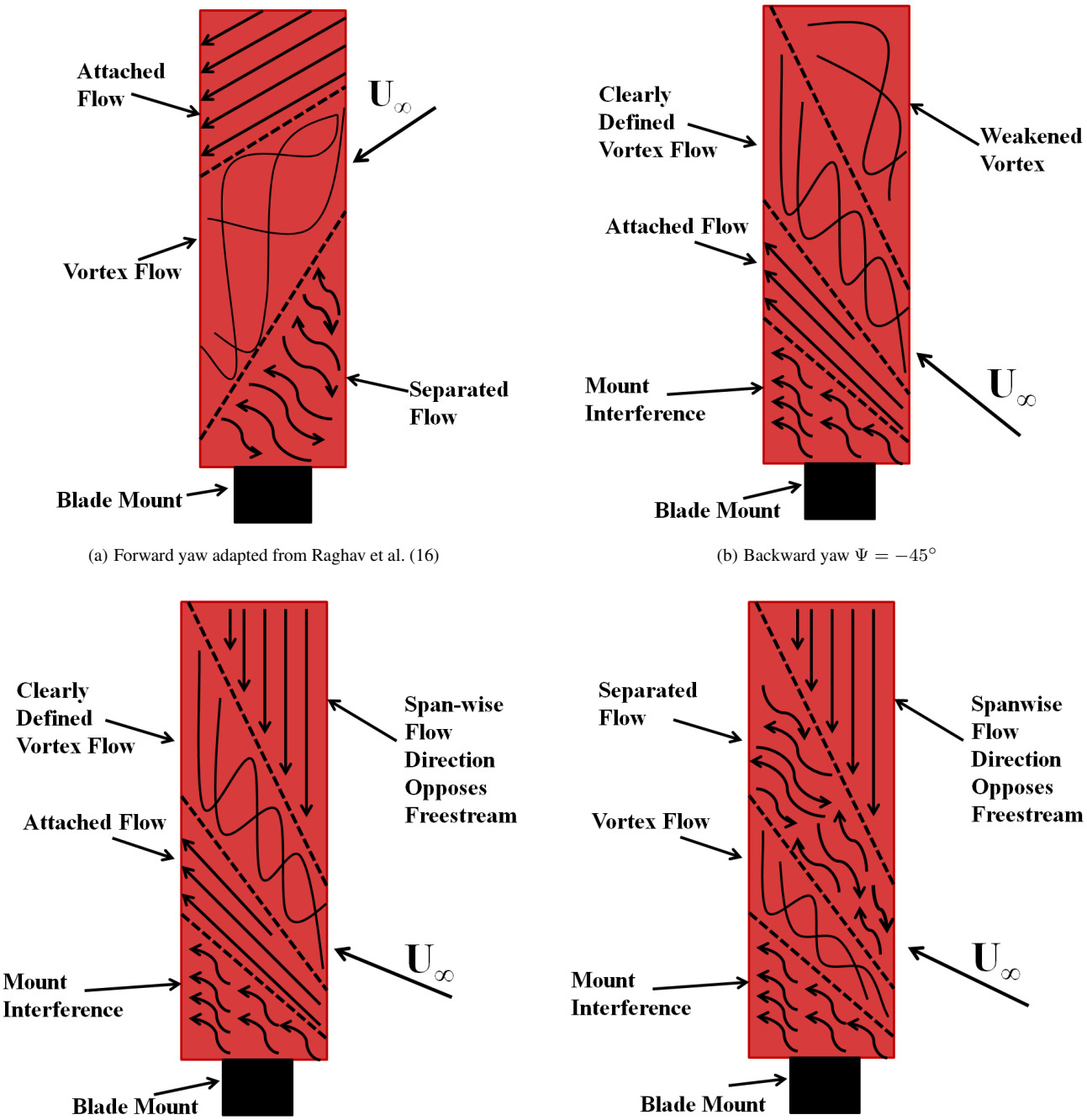

(a) Forward yaw adapted from Raghav et al. (16)

(b) Backward yaw $\Psi = -45°$

(c) Backward yaw $\Psi = -30° \alpha = 195° - 205°$

(d) Backward yaw $\Psi = -30° \alpha = 210° - 220°$

Fig. 7. Proposed flow topologies for a rotor blade in reverse flow

Raghav et al. (16) proposed a flow topology for a static forward yawed blade in the reverse flow regime. The flow topology shows three distinct flow regimes – attached flow, vortex flow, and separated flow demarcated by the dashed lines (see Figure 7(a)). In this section, we present generalized flow topologies for a static backward yawed blade in the reverse flow regime (see Figures 7(b)–7(d)). Clearly, the surface flow topology for a backward yawed blade differs significantly from that for a forward yawed blade in reverse flow regime. Furthermore, unlike for a forward yawed blade the surface flow topology on a backward yawed blade also changes with yaw angle and angle of attack. At $\Psi = -30°$ the surface flow topology consists of the familiar vortex and attached flow in addition to regions of span-wise flow in direction opposite to the expected span-wise flow. In the case of $\Psi = -30°$ the flow topology also changes with angle of attack as observed from Figures 7(c)–7(d). The effect of yaw angle on the flow topology is observed by comparing Figure 7(b) to Figures 7(c)–7(d). At the time of this writing it is not clear what causes these flow topology variations at the various conditions. Global velocity field measurements could be used to shine light on this behavior.

Given that the forward yaw flow topology regimes are fairly comparable over the range of yaw angles, it is amenable to be used for further analysis of the physics of the flow field. In this section we further analyze the variations in the flow topology for the forward yawed static blade at two different yaw angles as the angle of attack of the blade changes. We first present the variations in the area occupied by the different flow regimes with angle of attack followed by the analysis of the data.

Figures 8(a) and 8(b) illustrate the variation of the area occupied by each flow regime as a function of angle of attack for forward yaw angles at $Re = 1.7 \times 10^5$. An insignificant portion of the blade area (<10%) is typically occupied by the tip vortex interaction region and has not been presented in the figures. The salient features of each flow regime are clearly observed in the figures: a) for $\Psi = 30°$ the attached and vortex flow regimes monotonously decrease with an increase in angle of attack, while the unattached flow increases with angle of attack. b) At $\Psi = 45°$ the attached flow still exhibits a monotonous decrease with increase in angle of attack, however, the vortex and unattached flow regimes reach an equilibrium as angle of attack increases.

In order to further understand the behavior of the flow regimes with change in yaw angle and angle of attack, we shall consider the classical vorticity transport equation for an incompressible, barotropic fluid with conservative body forces (25). The following equations are defined as per the blade fixed coordinate axes defined in Figure 1:

$$\frac{\partial \boldsymbol{\omega}}{\partial t} = -\boldsymbol{v} \cdot \nabla \boldsymbol{\omega} + \boldsymbol{\omega} \cdot \nabla \boldsymbol{v} + \nu \nabla^2 \boldsymbol{\omega} \tag{3}$$

where the term representing the diffusion of vorticity due to viscous effects, $\nu \nabla^2 \boldsymbol{\omega}$, can be neglected based on the argument that the Reynolds number is sufficiently high. In addition, for simplicity of the argument if we neglect the vortex stretching/tilting term, $\boldsymbol{\omega} \cdot \nabla \boldsymbol{v}$, we arrive at a balance between span-wise vorticity (ω_z) production and advection terms, such that:

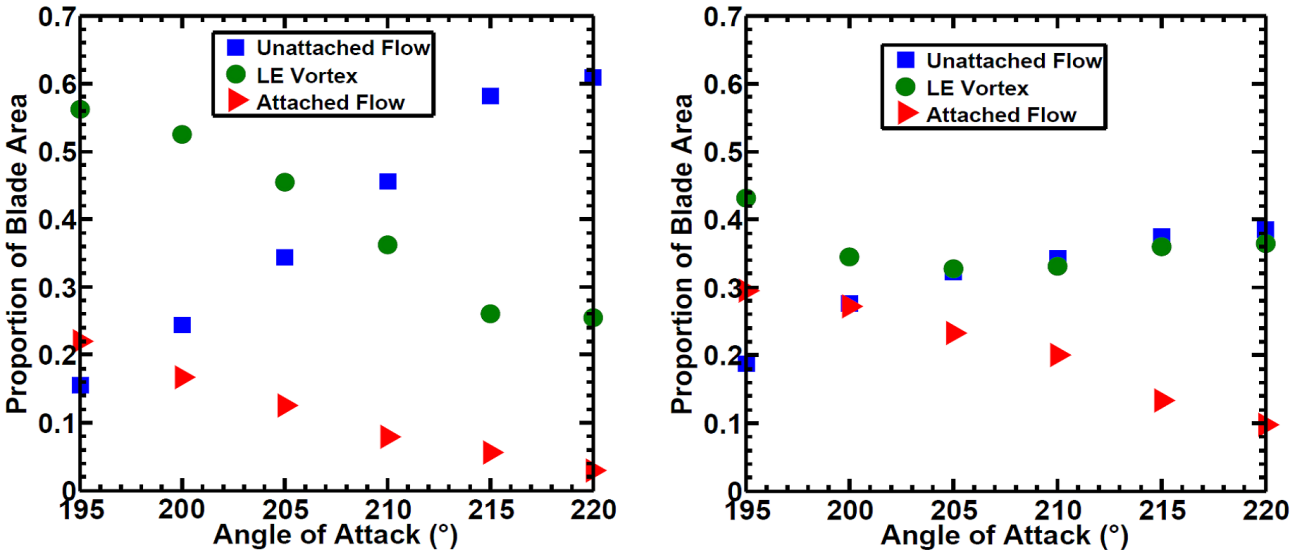

(a) $\Psi = 30°$ (b) $\Psi = 45°$

Fig. 8. Proportion of blade area occupied by the different flow regimes as a function of angle of attack at Re = 1.7×10^5

$$\frac{\partial \omega_z}{\partial t} + u\frac{\partial \omega_z}{\partial x} + v\frac{\partial \omega_z}{\partial y} + w\frac{\partial \omega_z}{\partial z} = 0 \tag{4}$$

From the surface flow visualization it can be clearly observed that the tufts indicate a predominant span-wise velocity w, with negligible velocity in the x_b and y_b directions u and v . The only terms that remain in equation 4 are the vorticity production term and the advection term in the z_b direction, such that $\frac{\partial \omega_z}{\partial t} + w\frac{\partial \omega_z}{\partial z} = 0$. Considering this simplified vorticity transport equation, it can be postulated that for greater yaw angles, an equilibrium state can be achieved as long as the vorticity produced at the leading-edge is rapidly advected away in the span-wise direction. This argument is now used to justify the equilibrium state that is achieved at the greater yaw angle $\Psi = 45°$ as observed in Figure 8(b) when compared to the lower yaw angle $\Psi = 30°$ as observed in Figure 8(a). At $\Psi = 45°$ the expected span-wise velocity is greater (by virtue of higher yaw angle) than at $\Psi = 30°$ and hence the equilibrium state is easily achieved. It should be noted that equation 3 does not include the term that accounts for destruction of vorticity due to annihilation. The influence of annihilation on the reverse flow aerodynamics is yet to be ascertained from quantitative flow field measurements.

5. Conclusions

A NACA 0013 rotor blade model was tested in regular flow and reverse flow regimes at various yaw angles and Reynolds numbers. Lift curves, drag polars, and pitching moments were analyzed from low-pass filtered, multi-axis load cell data. The Polhamus suction analogy for delta wings was adapted for application to a yawed rotor blade, and the predictions from the mathematical model were compared to experimental results. Flow tuft visualization was performed at various yaw angles and Reynolds numbers to reconcile the aerodynamic loads data. The conclusions follow:

1. The reverse flow lift curve slopes were higher than the corresponding regular flow lift curve slopes at forward yaw angles. The reverse flow lift curve slopes at backward yaw angles were lower than the reverse and regular flow lift curve slopes at forward yaw angles and did not follow the expected $\cos^2\Psi$ fit. The observed flow behavior of the backward yaw cases also differed significantly from the forward yaw cases. The lift asymmetry between the forward and backward yaw angles could affect trim conditions in very high advance ratio flight. It is important to note that mount interference could have influenced test results for the backward yaw angle cases, which represent a helicopter blade in the rotor azimuth regime $\Psi \geq 270°$.

2. The lift predictions made by the Polhamus delta wing equations showed excellent correlation with experimental results at forward yaw angles of $\Psi \geq 30°$. The Polhamus equations showed fair correlation at $0° \leq \Psi < 30°$, which is to be expected. The ability of the Polhamus equation to accurately predict static loads in the reverse flow regime set the stage to separate out the effects of rotation, from experiments on a rotating blade.

3. Drag polars showed that the regular flow regime produced higher L/D values than the reverse flow regime for the yawed rotor blade. Pitching moment data suggests that the chordwise center of pressure is near 0.75c in the reverse flow regime. The larger aerodynamic loads in the reverse flow region (as evidenced by the higher lift curve slopes) coupled with this shifted center of pressure would result in high torsional loads and pitch link loads during flight in the reverse flow regime.

4. Surface tuft flow visualization showed strong evidence of an attached leading edge vortex in the reverse flow regime. The vortex size was strongly dependent on the angle of attack and correlated well to the aerodynamic loads observed at the same yaw angle. The attached vortex contributes to higher blade loading in the reverse flow regime. The position and shape of the attached vortex closely resembled the "reverse-chord dynamic stall" vortex predicted by CFD for the slowed UH-60 rotor test (14). This suggests that the vortex may not be an artifact of rotation.

5. The flow topology over the forward yaw blade in reverse flow has three main regimes: the vortex, attached and separated flow at all the forward yaw angles tested. However, the flow topology over the backward yawed blade in reverse flow changes with yaw angle and angle of attack. Further velocity field measurements are necessary to understand this behavior.

6. The flow topology variation with yaw angle for a forward yawed blade suggests that at a greater yaw angle configuration the size of the attached span-wise vortex attains a maximum equilibrium value when compared to the lower yaw angle configuration. This observation is justified by using a vorticity transport analysis of the flow field.

Acknowledgements

This work was funded by the US Army Research office under grant number W911NF1010398. Dr. Frederick Ferguson is the Technical Monitor. The authors would like to thank Rafael Lozano for help with the fabrication of the experimental setup; Nicholas Mothahari and Oscar Pierre for their help with the data acquisition and post-processing.

References

[1] Mayo M, Motahari N, Raghav V, Komerath N. Vortex Flow Hypothesis for Rotor Blades in Reverse Flow. In: Proceedings of ASME 2013 International Mechanical Engineering Congress Exposition; 2013. .

[2] Walsh D, Weiner S, Arifian K, Lawrence T, Wilson M, Millott W, et al. High Airspeed Testing of the Sikorsky X2 TechnologyTM Demonstrator. In: American Helicopter Society 67th Annual Forum, Virginia Beach, VA; 2011. .

[3] Datta A, Yeo H, Norman TR. Experimental Investigation and Fundamental Understanding of a Full-Scale Slowed Rotor at High Advance Ratios. Journal of the American Helicopter Society. 2013;58(2):1–17.

[4] Lind AH, Lefebvre JN, Jones AR. Experimental Investigation of Reverse Flow over Sharp and Blunt Trailing Edge Airfoils. 2013;.

[5] Ewans J, Krauss T. Model Wind Tunnel Tests of a Reverse Velocity Rotor System. DTIC Document; 1973.

[6] Bagai A. Aerodynamic Design of the X2 Technology Demonstratorâ,,¢ Main Rotor Blade. In: American Helicopter Society 64th Annual Forum, Montreal, Quebec, Canada; 2008. .

[7] Ruddell AJ. Advancing Blade Concept (ABCâ,,¢) Development. Journal of the American Helicopter Society. 1977;22(1):13–23.

[8] Wheatley JB, Hood MJ. Full-Scale Wind-Tunnel Tests of a PCA-2 Autogiro Rotor. National Advisory Committee for Aeronautics; 1935.

[9] Charles BD, Tanner WH. Wind tunnel investigation of semirigid full-scale rotors operating at high advance ratios. DTIC Document; 1969.

[10] MacCloud JL, Biggers JC, Stroub RH. An Investigation of Full-Scale Helicopter Rotors at High Advance Ratios and Advancing Tip Mach Numbers. National Aeronautics and Space Administration; 1968.

[11] Harris FD. Rotor Performance at High Advance Ratio; Theory versus Test. National Aeronautics and Space Administration; 2008.

[12] Kottapalli S. Performance and Loads Correlation of a UH-60A Slowed Rotor at High Advance Ratios. In: Proceedings of the American Helicopter Society Future Vertical Lift Aircraft Design Conference; 2012. .

[13] Yeo H. Investigation of UH-60A Rotor Performance and Loads at High Advance Ratios. Journal of Aircraft. 2012;50(2):576–589.

[14] Potsdam M, Datta A, Jayaraman B. Computational Investigation and Fundamental Understanding of a Slowed UH-60A Rotor at High Advance Ratios. In: American Helicopter Society 68th Annual Forum, Fort Worth, TX; 2012. .

[15] Lee EH, Park BH, Han YO, Kim JH. Investigation on Aerodynamic Behaviors at the Extreme Angle of Attack of Two-Dimensional Wing. In: 30th AIAA Applied Aerodynamics Conference, New Orleans, Louisiana; 2012. .

[16] Raghav V, Mayo M, Lozano R, Komerath N. Evidence of Vortex-Inudced Lift on a Yawed Wing in Reverse Flow. Proceedings of the Institution of Mechanical Engineers, Part G: Journal of Aerospace Engineering. 2014;.

[17] Polhamus EC. A concept of the vortex lift of sharp-edge delta wings based on a leading-edge-suction analogy. National Aeronautics and

Space Administration; 1966.

[18] Raghav V, Komerath N. An Exploration of Radial Flow on a Rotating Blade in Retreating Blade Stall. Journal of the American Helicopter Society. 2013;58(2):1–10.

[19] Shevell RS. Fundamentals of flight. Prentice Hall; 1989.

[20] Critzos CC, Heyson HH, Boswinkle Jr RW. Aerodynamic Characteristics of NACA 0012 Airfoil Section at Angles of Attack From 0 deg to 180 deg. DTIC Document; 1955.

[21] Johnson W. Helicopter theory. Courier Dover Publications; 2012.

[22] Bartlett GE. Experimental investigation of influence of edge shape on the aerodynamic characteristics of low aspect ratio wings at low speeds. Journal of the Aeronautical Sciences (Institute of the Aeronautical Sciences). 1955;22(8):517–533.

[23] Campbell JF. Augmentation of vortex lift by spanwise blowing. Journal of Aircraft. 1976;13(9):727–732.

[24] Anderson JD. Fundamentals of aerodynamics. vol. 2. McGraw-Hill New York; 2001.

[25] Batchelor GK. An introduction to fluid dynamics. Cambridge university press; 2000.